Applied Thermal Engineering 204 (2022) 117947

Contents lists available at ScienceDirect

Applied Thermal Engineering

journal homepage: www.elsevier.com/locate/apthermeng

Performance assessment of a rotary active magnetic regenerator prototype using gadolinium

M. Masche, J. Liang, K. Engelbrecht, C.R.H. Bahl *

Department of Energy Conversion and Storage, Technical University of Denmark (DTU), Anker Engelunds Vej B301, 2800 Kgs. Lyngby, Denmark

ARTICLE INFO

Keywords:
Magnetocaloric effect
Active magnetic regenerator
Gadolinium
Flow imbalance
Experiment

ABSTRACT

We present the experimental results for a rotary magnetocaloric prototype that uses the concept of active magnetic regeneration, presenting an alternative to conventional vapor compression cooling systems. Thirteen packed-bed regenerators subjected to a rotating two-pole permanent magnet with a maximum magnetic field of 1.44 T are implemented. It is the first performance assessment of the prototype with gadolinium spheres as the magnetocaloric refrigerant and water mixed with commercial ethylene glycol as the heat transfer fluid. The importance of various operating parameters, such as fluid flow rate, cycle frequency, cold and hot reservoir temperatures, and blow fraction on the system performance is reported. The cycle frequency and utilization factor ranged from 0.5 to 1.7 Hz and 0.25 to 0.50, respectively. Operating near room temperature and employing 3.83 kg of gadolinium, the device produced cooling powers exceeding 800 W at a coefficient of performance of 4 or higher over a temperature span of above 10 K at 1.4 Hz. It was also shown that variations in the flow resistance between the beds could significantly limit the system performance, and a method to correct those is presented. The performance metrics presented here compare well with those of currently existing magnetocaloric devices. Such a prototype could achieve efficiencies as high as conventional vapor compression systems without the use of refrigerants that have high global warming potential.

1. Introduction

Magnetocaloric cooling systems are based on the active magnetic regenerator (AMR) cycle, which exploits the magnetocaloric effect (MCE) of ferromagnetic materials. The MCE describes the reversible temperature change when the material is adiabatically exposed to a changing external magnetic field. By applying a magnetic field, the magnetic moments of the atoms are aligned, causing the ferromagnetic material to heat up, and, correspondingly, the material cools down upon removal of the magnetic field. Magnetic heating and cooling have the possibility of a very efficient refrigeration process. Although the MCE was discovered almost 104 years ago by Weiss and Piccard [1], it took another 59 years for Brown [2] to demonstrate the first prototype of a magnetic heat pump operating near room temperature. In his device, pure gadolinium (Gd) was used as the working substance, which exhibits a second-order phase transition (i.e., the MCE) near room temperature [3,4]. Since then, the AMR concept has been brought to life, with a number of recent prototypes operating at different temperatures with Gd alloys as the magnetocaloric material [5–16].

Commonly, the performance of the AMR cycle is evaluated in terms of the cooling power ($\dot{Q}_c$) as a function of the reservoir temperature span (ΔT), which is the difference between the temperatures of the hot and cold reservoirs, T_{hot} and T_{cold}, respectively. Other widely used parameters to characterize the performance are the maximum cooling power ($\dot{Q}_{c,max}$) at zero span, the maximum temperature span (ΔT_{max}) at no load, and the coefficient of performance (*COP*), which is the ratio of cooling power to total net input power. In the following, the most relevant rotary AMR prototypes are briefly reviewed. In 2010, a rotary AMR device with a maximum field strength (B_{max}) of 1.47 T and two beds filled with 0.11 kg of Gd demonstrated a $\dot{Q}_{c,max}$ of 50 W over a 10 K span with a *COP* of 0.3–0.5 at 4 Hz and a ΔT_{max} of 29 K at no load [5]. The AMR achieved a maximum *COP* of 1.6 while providing a $\dot{Q}_c$ of 50 W over a 2.5 K span and at 1.4 Hz. Employing a modified magnet circuit (B_{max} = 1.54 T) and 0.65 kg of Gd particles, the ΔT_{max} at no load increased to 33 K at 0.8 Hz, and a $\dot{Q}_{c,max}$ of 96 W was obtained [17].

In 2012, a 1.24 T rotary AMR prototype achieved a ΔT_{max} of 25.4 K at no load and a $\dot{Q}_c$ of 100 W at a 20.5 K span at 2 Hz using 2.8 kg of Gd spheres filled into 24 beds. The largest *COP* was 1.8 for a $\dot{Q}_c$ of 400 W and a span of 8.9 K at 1 Hz [6]. In 2013, further experiments yielded a

* Corresponding author.
E-mail addresses: marv@dtu.dk (M. Masche), chrb@dtu.dk (C.R.H. Bahl).

https://doi.org/10.1016/j.applthermaleng.2021.117947
Received 20 September 2021; Received in revised form 4 December 2021; Accepted 11 December 2021
Available online 16 December 2021

Nomenclature

Acronyms

AMR	Active Magnetic Regenerator
DTU	Technical University of Denmark
MCM	Magnetocaloric Material
MCE	Magnetocaloric Effect
SOPT	Second-Order Phase Transition

Roman symbols

B	Magnetic flux density [T]
c	Specific heat capacity [J·kg^{-1}·K^{-1}]
COP	Coefficient of Performance [–]
d	Diameter [μm]
f	Operating (motor) frequency [Hz]
$\dot{e}_{xc}$	Specific exergetic cooling power [W·kg^{-1}]
$\dot{E}_{xc}$	Exergetic cooling power [W]
F_b	Blow fraction [%]
m	Mass [kg]
p	Pressure [bar]
$\dot{q}_c$	Specific cooling power [W·kg^{-1}]
$\dot{Q}_c$	Cooling power [W]
T	Temperature [K]
T_{cold}	Cold reservoir temperature [K]
T_{hot}	Hot reservoir temperature [K]
u	Relative standard uncertainty [%]
U	Utilization factor [–]
$\dot{V}$	Volumetric flow rate [L/h]
$\dot{W}_{losses}$	Iron losses [W]
$\dot{W}_{mag}$	Magnetic power into regenerator [W]
$\dot{W}_{shaft}$	Shaft power [W]
$\dot{W}_{pump}$	Pumping power [W]

Greek symbols

Δp	Pressure drop [bar]
ΔT	Temperature span, $T_{hot} - T_{cold}$ [K]
η_{II}	Second-law efficiency [%]
ρ	Density [kg·m^{-3}]
Γ	Shaft torque [Nm]
τ	AMR cycle period [s]
τ_b	Single blow period [s]

Subscripts

f	Fluid
max	Maximum
P	Particle

zero-span $\dot{Q}_{c,max}$ of 1010 W at 1.8 Hz. Notable temperature spans of 18.9 K and 13.8 K were obtained at 1.5 Hz for a heat load of 200 W and 400 W, respectively [15]. A maximum second-law efficiency ($\eta_{II,\max}$) of 5.6 % was obtained at 1.5 Hz for a 12.9 K span and a $\dot{Q}_c$ of 400 W, which corresponds to a *COP* of 1.23 [12]. Later, Okamura and Hirano [18] reported a $\dot{Q}_{c,max}$ of 200 W and a COP_{max} of 2.5 at a 5 K span for a 1.1 T AMR using 1 kg of Gd. Another prototype with a 0.85 T permanent magnet assembly achieved a ΔT_{max} of 13.8 K and a $\dot{Q}_{c,max}$ of 200 W, employing about 1.3 kg of Gd [19]. Also in 2013, a hybrid magnetic refrigerator combined with a Stirling gas refrigerator was proposed that comprised a Halbach cylinder ($B_{max} = 1.5$ T) and 198 g Gd sheets. Tests with He gas as the heat transfer fluid yielded a ΔT_{max} of 21.5 K at no load and a $\dot{Q}_c$ of 6 W at a 14.9 K span [20]. In 2014, a rotary AMR device with a permanent magnet that could induce a B_{max} of 1.17 T provided a ΔT_{max} of 38 K and a $\dot{Q}_{c,max}$ of 300 W with AMRs filled with Gd [19]. In the same year, a rotary AMR with $B_{max} = 1.25$ T and 1.2 kg of Gd provided a ΔT_{max} of 13.5 K at no load at a cycle frequency of 0.72 Hz [21]. Further testing demonstrated a ΔT_{max} of 11.9 K at no load at 0.93 Hz and a COP_{max} of 2.5 for a $\dot{Q}_{c,max}$ of 200 W close to zero span at 0.38 Hz [11]. The 1.5 T AMR built by Cheng et al. [22] produced a $\dot{Q}_{c,max}$ of 147 W and a ΔT_{max} at no load above 25 K at 2 Hz, employing 1.5 kg of Gd and GdEr particles.

In 2016, Trevizoli et al. [23] reported a $\dot{Q}_{c,max}$ of 53.7 W at zero span and 1 Hz and a ΔT_{max} of 28 K at 0.5 Hz for a 3.6 W $\dot{Q}_c$, employing a single packed-bed regenerator filled with 196 g of Gd. A peak *COP* of 4.6 was calculated when the AMR provided a $\dot{Q}_c$ of 11 W over a 5 K span and at 0.25 Hz, while a $\eta_{II,\max}$ of 13.5 % was obtained for a $\dot{Q}_c$ of 6.5 W over a 15 K span and at 0.25 Hz. The AMR used a magnetic circuit with a peak magnetic field of 1.69 T [24]. Moreover, Trevizoli et al. [25] found that the heat gain from the ambient to the regenerator is the main factor in reducing the AMR performance, underscoring the importance of a well-insulated AMR design. In the same year, a rotary AMR with $B_{max} = 1.6$ T and two regenerators with 0.25 kg Gd particles demonstrated a maximum cooling power of 18 W over a 3 K span and a ΔT_{max} of 21 K [26]. Another AMR with a rotor–stator magnetic circuit ($B_{max} = 1.0$ T) and eight pairs of beds, all filled with 1.7 kg of Gd, produced a ΔT_{max} of 12 K at 1 Hz and a $\dot{Q}_{c,max}$ of 150 W. The highest *COP* of 0.54 and $\eta_{II,\max}$ of 1.16% were obtained at a 7.1 K span at 0.8 Hz and for an 80.4 W $\dot{Q}_c$ [27]. Eriksen et al. [10] reported the performance of a rotary AMR device with $B_{max} = 1.13$ T and eleven regenerators filled a total of 1.7 kg of spheres made of Gd and $Gd_{(1-x)}Y_x$. At 0.75 Hz, the AMR demonstrated a ΔT_{max} of 20 K at no load and a $\dot{Q}_{c,max}$ of ca. 140 W over a span of around 5.5 K with a *COP* of 4.6. Later, this device demonstrated a $\eta_{II,\max}$ of 18% with a *COP* of 3.6 at a $\dot{Q}_c$ of 81.5 W at 0.61 Hz over a 15.5 K span [14]. Huang et al. [28] presented a 0.875 T rotary AMR, employing seven regenerators filled with a total of 1.18 kg of Gd. The device achieved a ΔT_{max} of 11.6 K at no load and at 1.7 Hz and a $\dot{Q}_{c,max}$ at zero span of 162.4 W with a *COP* of 1.59. The COP_{max} of 1.85 was obtained at 1.2 Hz for a $\dot{Q}_c$ of ca. 100 W. Recently, Lionte et al. [16] presented a high-performance AMR prototype with a permanent magnet system ($B_{max} = 0.51$ T) and 5.5 kg of Gd and Gd alloys, producing a $\dot{Q}_{c,max}$ of 900 W at an 18.4 K span with a *COP* of 9.7 and a $\dot{Q}_c$ of 768 W over a ΔT_{max} of 21.4 K with a *COP* of 8.4.

The present study describes experimental results for a rotary AMR device developed and built at the Department of Energy Conversion and Storage (DTU Energy). Depending on the specific needs of the application, the AMR device is able to provide a cooling or heating load [29]. The cooling/heating load can be measured at different operating conditions, e.g., hot reservoir temperatures, fluid flow rates, cycle frequencies, and blow fractions. A special focus has been directed to the hydraulic system operation and control, which are important factors in obtaining the optimum performance of the AMR cycle. Several studies [30–35] highlight that flow imbalance effects can harm the cooling performance of small-scale AMR devices, and corrective valve adjustments demonstrate performance improvements [31]. The effect of flow balancing in large-scale AMR devices with multiple regenerator beds has not been extensively studied. Hence, this study was also aimed at exploring the potential benefits of active valve control.

2. Experimental apparatus

A schematic section view and a photograph of the experimental apparatus are shown in Fig. 1. The apparatus was constructed as a rotary-type AMR, comprising a rotating two-pole permanent magnet, 13

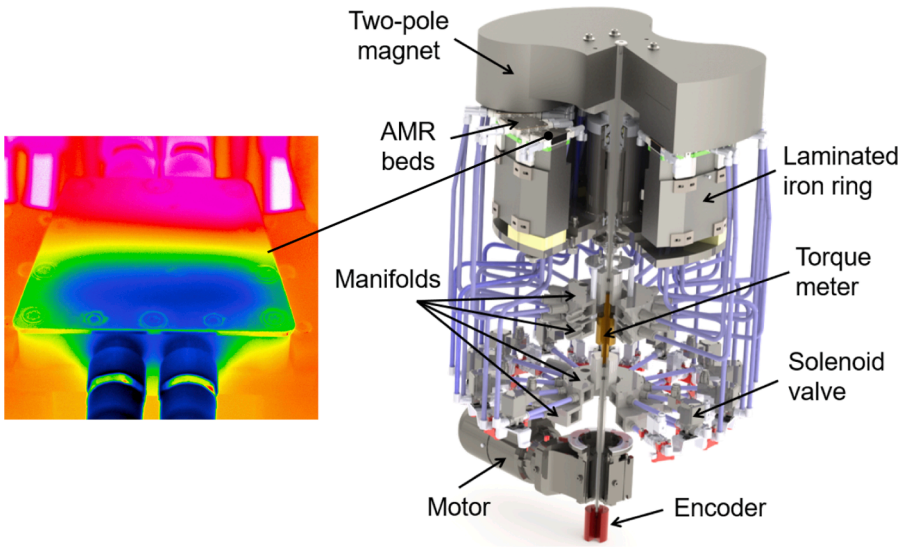

Fig. 1. Schematic section view of the AMR prototype. The inset shows an infrared image of an AMR bed during operation, making the cold and hot sides of the AMR bed visible.

fixed trapezoid-shaped regenerator beds, and a parallel flow circuit. The magnet produced by Bakker Magnetics is driven by an electric motor (NORD Drivesystems SK 92172.1 A), and it provides a maximum magnetic flux density of 1.44 T in the two high-field regions and close to 0 T in the two low-field regions. The flow circuit consists of 13 hot inlet solenoid valves (ASCO SCE238), 13 hot outlet solenoid valves (SMC 33VX232FGAXB), 26 check valves (SMC XTO-674) mounted on the regenerator cold side, four manifolds (i.e., two hot-side and two cold-side manifolds), and a centrifugal pump (Grundfos CRNE 1–9). According to the manufacturer, the opening and closing response times of the inlet valves are less than 25 and 40 ms, respectively, while the opening and closing response times of the outlet valves are 40 ms. The valves allow to remotely control the fluid flow through each regenerator, synchronized with the magnetic field. The pump circulates the heat transfer fluid, which is a mixture of 90 vol% deionized water and 10 vol % mono-ethylene glycol (automotive antifreeze) and connects the AMRs with the external (heat sink and heat source) heat exchangers. After the hot-to-cold blow (i.e., the hot blow), the fluid exiting the regenerator at the cold end flows through an electric circulation heater to absorb a cooling load, realizing the T_{cold}. The circulation heater installed on the cold end is used to evaluate the cooling capacity of the device. The warm fluid leaving the regenerator at the hot end after the cold-to-hot blow (i.e., the cold blow) passes through a chiller, which controls the T_{hot}. The difference between the cold and hot reservoir temperatures is then referred to as the established temperature span of the AMR apparatus. More details on the design components and operation of the magneto-caloric prototype are presented in [36] and [37], respectively.

The chiller (Julabo FL4003) and electric heater (Vulcanic DN 50) were adjusted to simulate different loading conditions. Flow rate, system pressure, magnet position, and shaft torque were monitored continuously using a flow meter (OMEGA FPR 200), pressure transmitters (Nöding Meßtechnik P20-408–1110), a rotary encoder (Hohner HS10), and a torque meter (Burster 8645–5175), respectively. Continuous measurements of the fluid temperature were performed inside the four manifolds and at the regenerator cold outlet ($T_{cold,out}$) using resistance thermometers (Pt100) and thermocouples (OMEGA Type E), respectively. The locations of the pressure and temperature measurements are indicated in Fig. 2. The percentage of the solenoid valve opening was controlled by the encoder angle. Hence, the blow fraction (F_b) can be determined [38]:

$$F_b = \frac{2\tau_b}{\tau}, \tag{1}$$

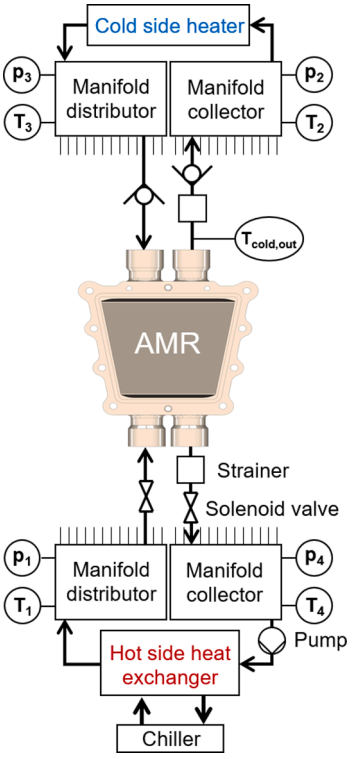

Fig. 2. Simplified fluid flow schematic of the system.

Where τ_b and τ denote the periods of a single fluid blow and the whole AMR cycle, respectively. The fluid flow and magnetic field profiles are given in Ref. [37].

Each of the 13 AMR beds was filled with 295 g of commercial-grade Gd spheres as the refrigerant. The material was collected from different sources but with similar properties. The diameter of the spheres was between 0.35 and 0.71 mm. A peak value of the specific entropy change in a 1 T field of 3.5 J/kg/K was measured at a peak temperature of 290.5 K. A total mass of 3.83 kg was used in the 13 tapered regenerator beds.

To ensure that the beds were filled properly and to assess the difference in flow resistance between them, the pressure drop along the

packed beds was measured over a range of flow rates and compared to the empirical Ergun equation [39] for flow in a packed bed with smooth particles [40]. Fig. 3 shows the measured and predicted pressure drop data. The pressure drop was defined as the difference between the pressure at the inlet (cold side) and outlet (hot side) of the bed. Preliminary tests showed no difference in the pressure drop between pumping the fluid in the converging (cold blow) or diverging (hot blow) direction of the regenerator housing. Hence, the measured data only shows the data for the converging flow. A needle valve was used to control the flow rate of the heat transfer fluid, and a pressure gauge was used to monitor the pressure response. Therefore, only horizontal boxplots are shown. Fig. 3 shows that the flow rate needed to obtain a specific pressure drop through each bed varied, indicating differences in the flow path resistances among the beds. The manual filling of the magnetocaloric material (MCM) and differences in fittings, tubing, and housing may explain the flow variations between the AMR beds. Overall, the average porosity was calculated to be 38.1 (±0.3)%, defined as the ratio of pore volume to regenerator (bulk) volume.

The measured pressure drop lies well between the pressure drop curves predicted by the Ergun equation for the lower and upper ends of the particle size range. The experimental data best fits the Ergun equation with a particle size of 500 μm. It should be noted that the dynamic viscosity of an ethylene glycol-based water mixture is larger than pure water [41]. This presents a pronounced increase in viscous losses and a larger pressure drop across the bed, which results in higher pumping power and hence decreases the device performance compared to pure water as a heat transfer fluid [42].

3. Thermodynamic performance

The thermodynamic performance of the AMR device is characterized as a refrigerator in terms of the cooling capacity ($\dot{Q}_c$), the second-law efficiency (or exergy efficiency), and the cooling *COP*. The latter one is a useful figure of merit for the performance of the thermodynamic cycle, and it is calculated via:

$$COP = \frac{\dot{Q}_c}{\dot{W}_{mag} + \dot{W}_{pump}} \tag{2}$$

Where $\dot{Q}_c$ is the amount of heat removed from the cold reservoir and calculated as:

$$\dot{Q}_c = \dot{V}\rho_f c_f \Delta T_{cold}, \tag{3}$$

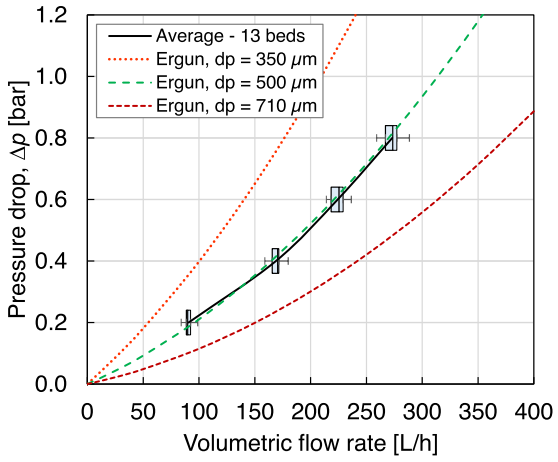

Fig. 3. Pressure drop along the 13 AMR beds as a function of the fluid flow rate compared to the predicted pressure drop by Ergun's equation. Boxplots indicate the median of the measured data between the first and third quartiles, and whiskers show the lowest and highest values.

Where ΔT_{cold} is the temperature difference of the fluid between the inlet and outlet of the electric circulation heater installed on the cold side, i.e., $T_3 - T_2$. c_f, ρ_f and $\dot{V}$ are the fluid specific heat capacity, fluid density, and volumetric fluid flow rate, respectively. The properties of the heat transfer fluid were calculated using the commercial software Engineering Equation Solver [43].

In the *COP* calculation, only the power contributions delivered to the magnetocaloric material are considered, i.e., the magnetic power ($\dot{W}_{mag}$) and the pumping power ($\dot{W}_{pump}$). The power consumption of the solenoid valves is external to the AMRs. Hence, losses associated with the flow distribution system are not included in the *COP* calculation. Furthermore, the solenoid valves are custom-designed and hence not optimized for the specific task, which explains their high power consumption of around 60 W [36] at a blow fraction of 36%. In future AMR designs, a more appropriate valve selection with fewer mechanical losses may reduce the valve power consumption and hence the system *COP*.

$\dot{W}_{pump}$ is the power needed to pump the working fluid through the AMR beds and hence accounts for the fluid friction irreversibilities. It is calculated as the product of fluid flow rate and pressure drop through the AMR device. It can be determined as follows:

$$\dot{W}_{pump} = \dot{V}(p_1 - p_2 + p_3 - p_4) \tag{4}$$

Where p_1, p_2, and p_3 are the fluid pressures measured in the three manifolds. The atmospheric pressure p_4 is assumed to be zero. An ideal pumping efficiency of 1 is assumed, as the pump is not optimized for operating at a specific flow rate. Instead, an efficiency should be considered when the pump is specifically designed for the intended use.

$\dot{W}_{mag}$ is the magnetic power performed on the regenerator material, and it is calculated from the measured shaft power ($\dot{W}_{shaft}$) needed to rotate the magnet. The power losses ($\dot{W}_{losses}$) associated with both eddy currents induced in the laminated iron ring and bearing and coupling friction are subtracted from the $\dot{W}_{shaft}$. Hence, we can write:

$$\dot{W}_{mag} = \dot{W}_{shaft} - \dot{W}_{losses} \tag{5}$$

Where $\dot{W}_{shaft}$ is determined by the following equation.

$$\dot{W}_{shaft} = 2\pi f \Gamma, \tag{6}$$

Where f is the operating frequency, which is half of the AMR (or cycle) frequency (f_{AMR}), as two high fields are generated by the magnetic circuit. Γ is the mechanical torque directly measured at the shaft.

When the AMRs were installed, the measured shaft power was about 60 W at a frequency of 1 Hz. Compared to a previous study [37] that applied multi-layered AMR beds filled with LaFeSi-based alloys, the shaft power was about 65 W at 1 Hz. The lower power in the present study is probably due to the more homogeneous material distribution in the single-layer Gd bed.

The power losses are a function of f_{AMR}, similarly, as shown in [37], and $\dot{W}_{losses}$ can then be approximated by a second-order polynomial:

$$\dot{W}_{losses} = \alpha {f_{AMR}}^2 + \beta f_{AMR}, \tag{7}$$

$$\alpha = 29.3 Ws^2,$$

$$\beta = 31.1 Ws.$$

Eddy currents induced in the iron core scale approximately quadratically with the cycle frequency, and friction scales approximately linearly [44]. Thus, the quadratic term of the second-order polynomial is taken to represent the power lost due to eddy currents induced in the laminated iron ring, and the linear term represents the power loss from friction in the bearings. The coefficient of the linear term (β) can be considered as an estimation of the total frictional moment. Generally, the power dissipated inside the bearings due to

friction depends on the bearing type, lubricant physical properties, shaft rotational speed, and the loads applied [45]. To minimize power losses due to eddy currents, the iron ring was built up from 23 laminations (each 4 mm thick). The eddy current loss coefficient (α) presents an estimation of the product of lamination thickness, total iron core volume, peak magnetic flux density, and electrical conductivity of the core material [44]. In the results and discussion section, we subtract the losses from the shaft power and just report $\dot{W}_{mag}$ as the magnetic or AMR power.

In order to calculate the second-law efficiency (or exergy efficiency), the ideal *COP* (COP_{ideal}) when expressed in the Carnot cycle needs to be defined first:

$$COP_{ideal} = \frac{T_{cold}}{T_{hot} - T_{cold}} \tag{8}$$

The second-law efficiency (η_{II}) can then be written as:

$$\eta_{II} = \frac{COP}{COP_{ideal}} \tag{9}$$

The exergetic cooling power ($\dot{E}_{XQ}$) is another performance metric for comparing refrigeration systems that combines the temperature span and the cooling power of the device. It is a measure of the ability of the AMR device to produce a useful cooling load, and it serves as the basis for evaluating the cost structure of a magnetocaloric refrigerator. For instance, if the exergetic cooling power is high, an AMR device with more costly components may yield cooling loads at lower costs than other devices with a lower cost structure [46]. Unlike the *COP* and the η_{II}, the exergetic cooling power is not influenced by the pressure drop.

$$\dot{E}_{xc} = \dot{Q}_c \left(\frac{T_{hot}}{T_{cold}} - 1 \right) = \frac{\dot{Q}_c}{COP_{ideal}} \tag{10}$$

The relative standard uncertainties (u) of the calculated performance parameters were estimated following the Taylor Series Method (TSM) [47] for propagation of uncertainties, combining both random and systematic uncertainties. The random uncertainty was calculated from the standard deviation of the measured data, while the systematic uncertainty refers to the accuracy in measuring an instrumentation sensor. The accuracies for the different sensors used are listed in [37]. The relative standard uncertainties of the performance parameters calculated in this study are summarized in Table 1. For the uncertainty of the magnetic power, we only considered the system uncertainty, as the variation of the torque (and hence power) measurements in the sampling period originates from the interaction between the magnetic circuit and the regenerator beds. In other words, the magnetization and demagnetization of the regenerator beds produce an alternating torque, similar to that shown in [23,48], and hence the power measurement variation is due to the AMR internal operation and not from random error sources [48,49]. All presented performance data were averaged over a period of 10 min after reaching steady-state operating conditions. All the experimental results presented in the following chapter are organized in an Excel spreadsheet in the Supplementary Material of this article. The spreadsheet can also be used as a design tool to evaluate the actual *COP* of a realistic AMR system.

4. Results and discussion

A large number of experiments have been carried out with the focus on improving the performance of the AMR device. For mapping the optimum AMR performance, the influence of various operating parameters has been studied. These parameters include the cycle frequency, volumetric flow rate, cold and hot reservoir temperatures, blow fraction, and timing between fluid flow profile and magnetic field profile (i.e., the AMR cycle timing). In general, the operating parameters for an AMR system need to be chosen carefully to ensure optimum performance. A key parameter governing the AMR performance is the utilization factor. It combines important operating parameters and relates the thermal capacity of the working fluid flowing through the regenerator during one blow (hot orcold blow) to the thermal capacity of the regenerator material:

$$U = \frac{\rho_f c_f \dot{V}}{2 f m_s c_s}, \tag{11}$$

Where c_s represents the average specific heat capacity of the refrigerant, which is set to $c_s = 380$ J kg^{-1} K^{-1}, as per [50]. The total mass of the MCM is $m_s = 3.83$ kg. The relative uncertainty of the calculated utilization factor is about 1.3%.

4.1. Effect of flow balancing

Fluid flow operation and control are important aspects in determining the optimum performance of the AMR device. The AMR performance reduction for an unbalanced flow system is shown in several studies [10,30,32,51]. In the present study, the 13 beds were filled manually, so small variations in the flow path resistance are present, i.e., the flow resistance through each bed is not equal. This is indicated by the boxplots in the measured data for the pressure drop in Fig. 3. Additionally, engineering tolerances in the production of fittings, tubing, and solenoid valves may contribute to uneven flow resistances between the AMR beds after mounting them on the experimental apparatus. In this study, flow imbalances in the multi-bed AMR device can be corrected by changing the percentage of the solenoid valve opening, which controls the blow fraction through each regenerator bed.

The temperature of the fluid exiting the regenerator at the cold end (i.e., the regenerator cold outlet temperature) can serve as an indicator of how well the flow is balanced, as shown by Eriksen et al. [30]. The authors found that an unbalanced flow had a significant impact on the temperature profile in the AMR bed, particularly on the regenerator cold outlet temperatures. Fig. 4 shows the regenerator cold outlet temperatures obtained when operating the device at a frequency of 0.8 Hz, average blow fractions of 36% in the cold blow and hot blow directions, a flow rate of ca. 600 L/h ($U = 0.30$), and cold and hot reservoir temperatures of 286 K and 301 K, respectively. It can be seen that the variation of $T_{cold,out}$ can be narrowed by adjusting the blow fraction of the hot outlet solenoid valves for beds that appear to have different flow

Table 1
Estimated relative standard uncertainties of the calculated performance metrics.

	$\dot{Q}_c$	$\dot{W}_{pump}$	$\dot{W}_{mag}$	ΔT	COP	η_{II}	$\dot{E}_{XQ}$
u [%]	9.8	2.7	1.5	1.0	9.8	9.9	9.8

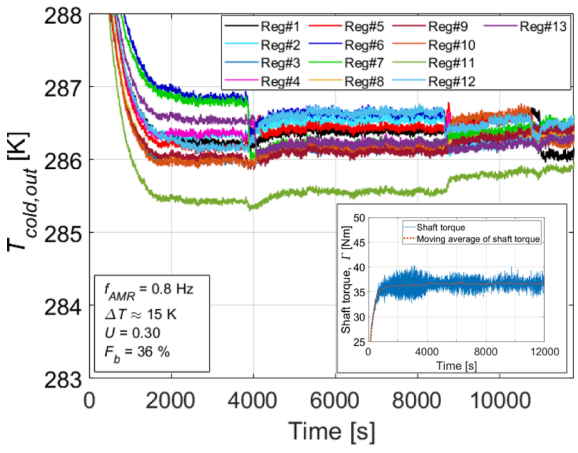

Fig. 4. Regenerator cold outlet temperatures measured after the hot-to-cold blow. The inset shows the effect of flow balancing on the shaft torque.

resistances. After reaching steady-state operation at 3800 s, the cold and hot blow fractions for beds #6, #7, and #11 were adjusted while maintaining the same utilization to bring their outlet temperature closer to the remaining beds. In particular, the hydraulic resistance of the flow path in bed #11 appears to be quite different from the rest. The adjustment of the three blow fractions modifies the bed outlet temperatures subsequently, as indicated in Fig. 4 at 4100 s. This is due to the parallel flow circuit configuration, i.e., multiple beds are constantly open to flow in the hot-to-cold direction during demagnetization and the cold-to-hot direction during magnetization. Therefore, from a fluid flow perspective, the flow for each bed interacts with a couple of other beds in both flow directions, resulting in interdependence of temperature profiles between beds. This narrowing of the outlet temperature was repeated for different beds until reaching a tolerable variation of the $T_{cold,out}$.

The effect of balancing the $T_{cold,out}$ on the shaft torque is shown in the inset in Fig. 4. An uneven flow distribution between the beds causes larger amplitudes of the shaft torque but only has a small influence on the average shaft torque. Table 2 summarizes the performance improvement obtained by balancing the $T_{cold,out}$ as a result of the control of individual valve blow fractions, i.e., the active valve control. For the given operating conditions, balancing reduced the spread of the average $T_{cold,out}$ ($\overline{T}_{cold,out}$) indicated by a lower standard deviation. At the same time, the cooling power and the *COP* increased from 150.9 W to 264.5 W and from 2.28 to 3.97, respectively. Overall, the balancing of the $T_{cold,out}$ represents a performance improvement of more than 70%, indicating that the active control of individual valve blow fractions can become an important method to improve the AMR cooling performance. Hence, this method of narrowing the cold outlet temperatures was done for each set of operating conditions to obtain the best AMR performance, and the data presented in the following sections are based on an adjusted flow.

4.2. Temperature evolution test

Fig. 5 shows a typical time evolution plot of the temperature for the heat transfer fluid leaving the external heat exchangers at the cold and hot reservoirs when operating the AMR system at a cycle frequency of 1.7 Hz, a utilization of 0.31, and an average blow fraction of 36% in the cold and hot blow directions. In addition, the established temperature span is presented. The hot and cold reservoir temperatures were set to approximately 301 and 285 K, respectively. Initially, the working fluid starts at ambient temperature (ca. 295 K) in the cold and hot reservoirs. Then, the cold fluid reservoir temperature decreases while the hot fluid reservoir temperature increases gradually until reaching steady-state conditions after around 1500 s (25 min). As the temperature span increases, higher shaft torque (and hence higher magnetic power) is required (see inset in Fig. 6), as both the AMR bed will become more ferromagnetic, causing an increased magnetic attraction, and the

Table 2
Selected steady-state average data connected to Fig. 4 demonstrating the effect of adjusting the regenerator cold outlet temperatures on the AMR performance. The plus-minus values indicate one standard deviation from the average (i.e., the random uncertainty).

Time [s]	$\overline{T}_{cold,out}$ [K]	ΔT [K]	$\dot{Q}_c$ [W]	$\dot{W}_{pump}$ [W]	$\dot{W}_{mag}$ [1] [W]	*COP* [-]
3800	286.2 ± 0.4	14.7 ± 0.1	150.9 ± 7.4	18.2 ± 0.4	47.8	2.28 ± 0.11
8500	286.3 ± 0.3	14.8 ± 0.1	236.9 ± 11.6	18.3 ± 0.4	48.4	3.55 ± 0.18
10,200	286.3 ± 0.2	14.8 ± 0.1	261.2 ± 12.7	18.2 ± 0.4	48.8	3.90 ± 0.19
11,800	286.3 ± 0.2	14.8 ± 0.1	264.5 ± 12.9	18.2 ± 0.4	48.4	3.97 ± 0.20

[1] Power measurement variations originate from the AMR internal operation and are not from random error sources.

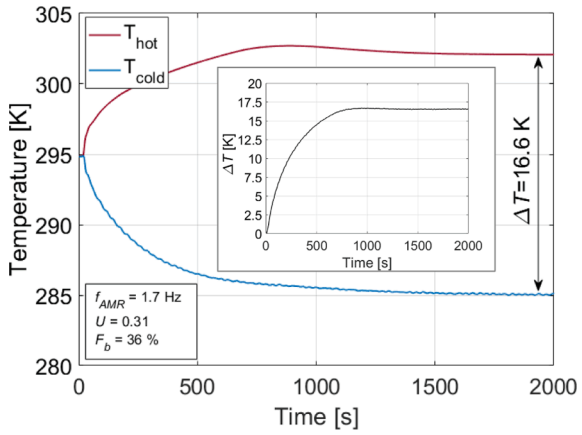

Fig. 5. Time evolution of the temperatures at the cold and hot reservoirs of the AMR system. The inset shows the established temperature span.

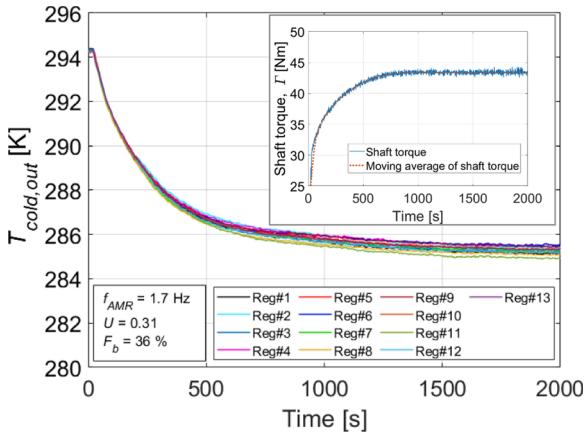

Fig. 6. Time evolution of the regenerator cold outlet temperatures and shaft torque (inset) until reaching steady-state conditions during testing of the magnetocaloric device.

thermodynamic work needed to transport heat over a larger span is greater. The established steady-state temperature span based on the reservoir temperatures is about 16.6 K. The regenerator temperature span, which is always greater than the reservoir temperature span [23] and based on the temperatures of the fluid exiting the regenerator on the cold and hot sides, is 17.1 K. Hence, the AMR system can achieve a quick temperature pull down for rapid cooling. In comparison, it took ca. 2 h for the AMR system developed by Naskashima et al. [52] to establish a regenerator temperature span of about 15 K.

The evolution of the cold side outlet temperatures exiting the 13 regenerator beds is shown in Fig. 6. It can be seen that during the temperature pull-down, the thermal window, i.e., the temperature range between the minimum and maximum regenerator cold outlet temperature, increases. After reaching a steady state, the thermal window is constant and ranges from 284.9 to 285.5 K. The established variation between the regenerator cold outlet temperatures may be attributed to differences in the flow resistance (flow balancing) inside the AMR beds (cf. Fig. 4).

4.3. Effect of utilization

Several studies have shown an optimum value of the utilization factor that provides maximum cooling capacity [7,23,27,53]. In the present study, the utilization factor was varied by changing the volumetric flow rate of the heat transfer fluid. Then, for each cycle frequency, the maximum AMR performance could be obtained at optimum

utilization. For example, Fig. 7a shows the cooling power and cooling *COP* as a function of the utilization factor for a cycle frequency of 0.5 Hz, an average blow fraction of 36% in the cold and hot blow directions, and cold and hot reservoir temperatures of 285 K and 301 K, respectively. The results show that the cooling power produced by the Gd-based AMR system is quite sensitive to the amount of heat transfer fluid (i.e., the utilization). The cooling power reaches a peak value at optimum utilization and then drastically drops with increasing utilization (volumetric flow rate). A small amount of heat transfer fluid (i.e., a low utilization) only produces a little cooling capacity, while excessive fluid (i.e., a high utilization) disturbs the AMR temperature profile and leads to a loss in cooling power. Similarly, the cooling *COP* drops drastically after passing the optimum utilization, which provides the maximum cooling capacity. At $U = 0.41$, the peak cooling power was about 181.1 W with a cooling *COP* of 3.2. It indicates that the utilization needs to be adjusted carefully to achieve optimal performance in terms of thermodynamic efficiency. Furthermore, Fig. 7b shows that the magnetic power dominates the required power input, and higher values of the utilization increase both the pumping power due to a larger pressure drop across the system and the magnetic power, which was also reported by Fortkamp et al. [38].

4.4. Effect of the hot reservoir temperature

A series of experiments was run to investigate the effect of the hot reservoir (or working) temperature on the AMR performance. The results presented in Fig. 8a were obtained at a fixed cycle frequency of 0.5 Hz, a flow rate of 500 L/h ($U = 0.39$), an average blow fraction of 36% in the cold and hot blow directions, and for different cold reservoir temperatures. In comparison to previously tested LaFeSi-based AMRs [37] that showed a great system performance dependence on the hot reservoir temperature, the performance of the Gd-based AMR system appears not to be largely influenced by the hot reservoir temperature. For example, at a constant temperature span of 14 K, the cooling powers and *COP*s are quite similar for both temperatures. Furthermore, Fig. 8b indicates that the effectiveness of the system relative to its performance in idealized conditions is not sensitive to the hot reservoir temperature. The cooling performance maps also show that the device operates more efficiently at higher cooling powers, and this is independent of the working temperature. A maximum second-law efficiency of 39.2% was calculated when the device was run at 0.5 Hz, a utilization of 0.39, and a hot reservoir temperature of 301 K. Under these conditions, the AMR produced a cooling power of 444.5 W over a 7.3 K span with a cooling *COP* of 15.9.

Fig. 9a illustrates the specific cooling capacity ($\dot{q}_c$) and second-law efficiency achieved by the AMR device as a function of the temperature span when employing Gd as the MCM. The maximum cooling performance of the same device using LaFeSi-based AMRs with ten different Curie temperatures and similar bed porosity is also presented [36]. The relationship between the specific cooling capacity and the temperature span is approximately linear when employing Gd-based and LaFeSi-based AMRs. It should be noted that the cooling characteristics for the Gd-based AMRs were obtained at a slightly higher utilization ($U = 0.39$) than for the La-based AMRs ($U = 0.34$). Running the AMR device with Gd at lower utilization, however, may lead to an even smaller inclination of the slope of the cooling line (cooling power vs. temperature span) [13]. The cooling performance of the LaFeSi-based AMRs, hence, drops more drastically, as indicated by a steeper slope of the cooling line, indicating that they may provide higher cooling capacities at a smaller temperature span. The Gd-based AMRs, on the other hand, demonstrate a better absolute cooling performance, as they provide higher cooling capacities and efficiencies at higher temperature spans under similar operating conditions. To illustrate the relative cooling performance of the different AMRs, the specific exergetic cooling power ($\dot{e}_{xc}$), which combines the specific cooling capacity and the temperature span of the AMR device, was plotted in Fig. 9b. The Gd-based AMRs show higher values of the $\dot{e}_{xc}$, and they outperform the LaFeSi-based AMRs over all specific cooling capacities. Thus, the most useful cooling is provided when the AMR device employs Gd as the working refrigerant. However, it should be noted that due to manufacturing variation, the Curie temperatures and the distribution of the Curie temperatures of the ten-layered LaFeSi-based AMRs were not as designed. Thus, the LaFeSi-based AMRs did not perform optimally.

4.5. Effect of the cycle frequency

The effect of changing the cycle frequency on the maximum AMR cooling capacity is summarized in Fig. 10a. The temperature span and hot reservoir temperature were fixed at approximately 16 K and 301 K, respectively, while the cycle frequency was varied. The maximum $\dot{Q}_c$ ($\dot{Q}_{c,max}$) and maximum *COP* (COP_{max}) were obtained at optimal utilization values varying between 0.26 and 0.37 depending on the cycle frequency. At each frequency, there exists an optimal value of the utilization where the cooling power can be maximized, as seen in Fig. 7a, exemplarily, and hence, the optimal U changes with frequency. An optimal value of U is attained when an effective heat transfer and a minimal reduction in the temperature gradient along the flow direction can be realized [55]. It can be seen that $\dot{Q}_{c,max}$ increases with frequency up to 1.4 Hz, which appears to be the optimum for the device. Although it was expected that higher frequencies would increase the cooling capacity further, the operation and control of the solenoid valves probably limit a higher performance at 1.7 Hz. The performance drop-off at 1.7 Hz may indicate that the AMR design has reached certain limitations, e.g., the fluid volume that was pumped through the device was limited, hence limiting the achievable cooling capacity. The highest power of 344 W

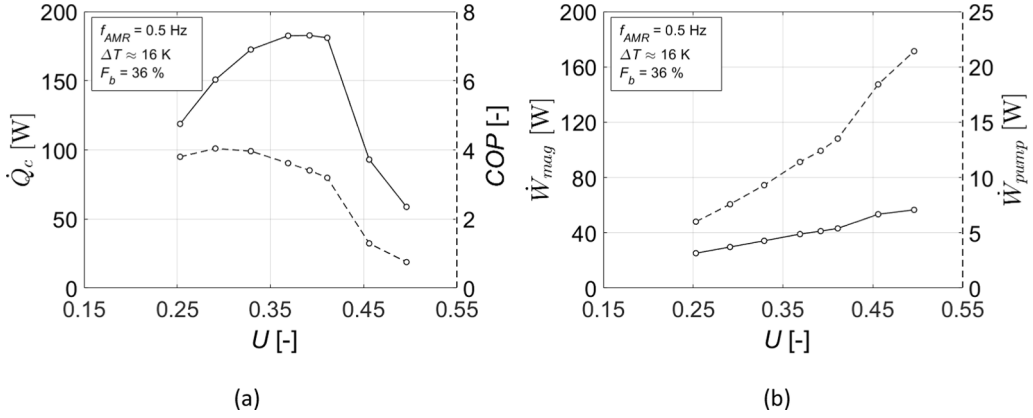

Fig. 7. (a) Cooling power (solid line) and cooling COP (dashed line) vs. the utilization factor. (b) Magnetic power (solid line) and pumping power (dashed line) vs. the utilization factor.

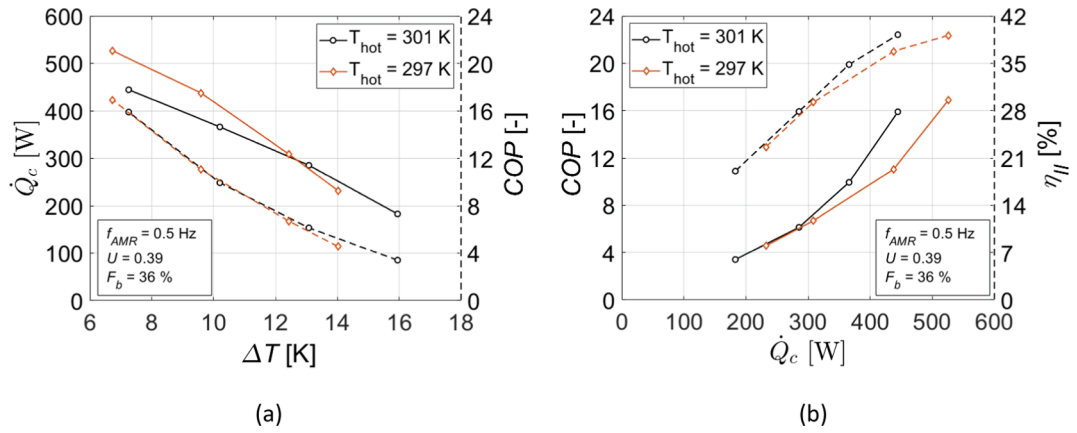

Fig. 8. (a) Cooling power vs. temperature span at different hot reservoir working temperatures. Cooling power is plotted with solid lines, while cooling COP is plotted with dashed lines. (b) Cooling performance maps (cooling COP vs. cooling power) for different hot reservoir temperatures. The cooling COP is plotted with solid lines, while the second-law efficiency is plotted with dashed lines.

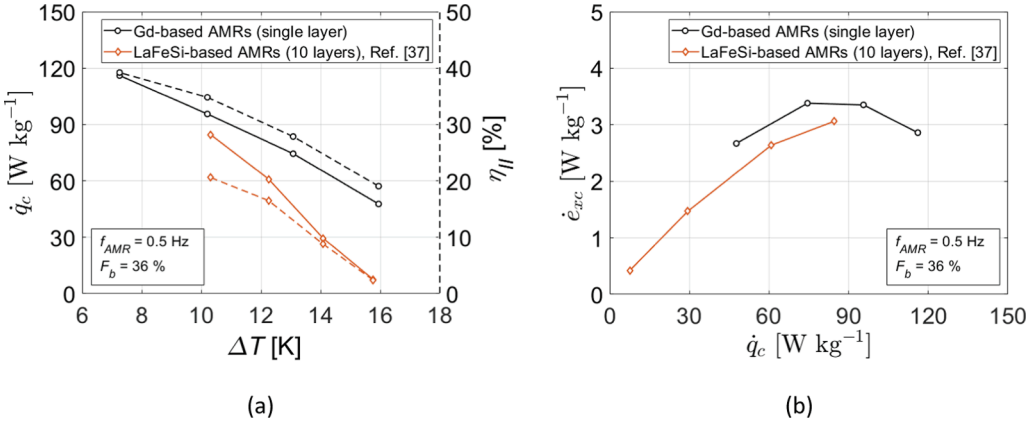

Fig. 9. (a) Comparison of the specific cooling power and second-law efficiency as a function of the temperature span for single-layered Gd and ten-layered LaFeSi-based AMRs. (b) Comparison of the specific exergetic cooling capacity as a function of the specific cooling capacity for single-layered Gd and ten-layered LaFeSi-based AMRs.

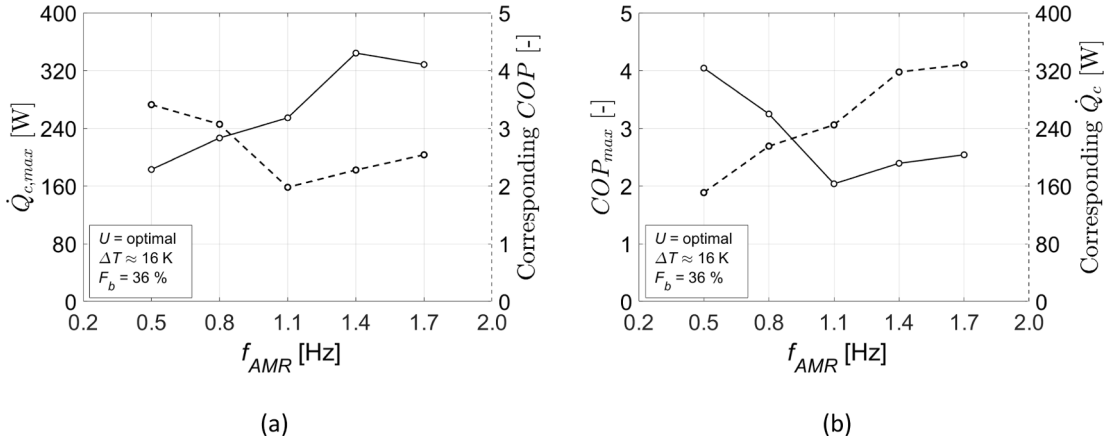

Fig. 10. (a) Maximum cooling power (solid line) and corresponding COP (dashed line) as a function of cycle frequency. (b) Maximum COP (solid line) and corresponding cooling power (dashed line) as a function of cycle frequency.

was obtained at 1.4 Hz and a utilization of 0.33 with a corresponding cooling *COP* of 2.3. At this condition, the second-law efficiency was 13.2%.

It is also obvious that the maximum *COP* decreases approximately at higher frequencies (Fig. 10b), which can be attributed to the larger power requirements of both the magnet motor and the centrifugal pump at higher frequencies (Fig. 11). As shown in Fig. 11, higher values of the utilization (larger flow rates) cause an increase in the pumping power due to a larger system pressure drop. Furthermore, by increasing the cycle frequency, the pumping power demand increases faster and at a

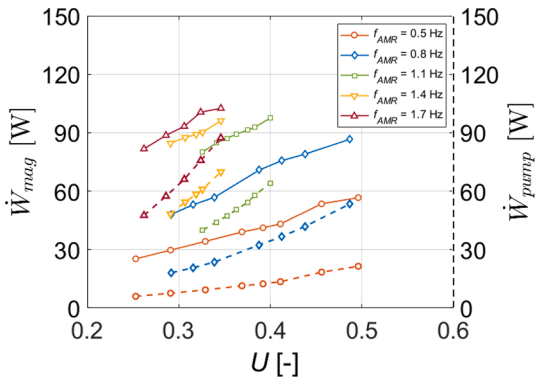

Fig. 11. Magnetic power (solid lines) and pumping power (dashed lines) as a function of utilization and cycle (AMR) frequencies.

steeper slope as a function of the utilization. This is attributed to the larger system pressure drop that occurs at higher volume flow rates. For instance, at a frequency of 0.5 Hz and $U = 0.33$ ($\dot{V} = 420$ L/h), the contributions of the pumping power and magnetic power to the total input power are 21.4 % and 78.6 %, respectively for the magnetic power. In comparison, at 1.7 Hz and $U = 0.33$ ($\dot{V} = 1410$ L/h), the fraction of the pumping power increased by about 120% and contributed to about 43% of the total AMR power, while the contribution of the fraction of the magnetic power decreased to 57%. Similar observations were made by Trevizoli et al. [23]. The AMR device will run more efficiently at lower cooling capacities because of fewer heat transfer irreversibilities and reduced magnetic and pumping power consumption. Moreover, the pumping power loss will outperform the heat transfer rate improvement at higher frequencies. Hence, the combined adjustment of the cycle frequency and fluid flow rate may become an important control strategy to realize part-load operating conditions with superior energy-saving potential [56].

4.6. Temperature spans at different cooling capacities

Finally, the system performance was evaluated for different applied cooling loads, which is crucial from a practical perspective. Fig. 12 presents the cooling curves (cooling power vs. temperature span) and cooling *COPs* at two cycle frequencies. The average blow fraction in the cold and hot blow directions was 36%. The hot reservoir temperature was fixed at 301 K, while the temperature of the cold reservoir and utilization factor (volume flow rate) were varied. A relatively linear relationship between the cooling power and temperature span was observed when using a single-layer Gd bed, and, as expected, the cooling power decreased with an increased temperature span. This means that higher cooling powers can be obtained at the expense of the temperature span. The linearity has also been validated both numerically and experimentally [8,13,57,58] although it was done to describe the relationship between the cooling power and temperature span. A noteworthy cooling power of about 818 W and a cooling *COP* of 4.2 were obtained at a cycle frequency of 1.4 Hz and a flow rate of 1650 L/h ($U = 0.46$) over a span of 10.1 K. At this condition, the second-law efficiency was 14.5% (Fig. 13). Higher utilizations (and hence higher flow rates) could not be tested, as they would cause a larger system pressure drop and subsequent shutdown of the system due to safety reasons. It should be pointed out that the temperature spans established by the AMR device are lower than some magnetocaloric prototypes [6,17,19,22,23,54,59–62]. Fig. 13 also indicates that increasing the utilization from 0.29 to 0.46 reduces the second-law efficiency by about 60% at a 14 K span and at 1.4 Hz, while the device running at 0.8 Hz can have a 20% improved second-law efficiency.

It also appears that the slope of the cooling curves increases as both the frequency and utilization increase. Hence, higher cooling powers can be obtained at higher utilization (and hence larger flow rate) and lower spans, while they decrease faster with increasing temperature span. The cooling line becomes steeper, as the utilization value increases, as also demonstrated in Ref. [54]. Thus, the maximum cooling capacity is largest at lower spans. Moreover, as expected, the AMR efficiency in terms of the cooling *COP* decreases with increasing utilization due to increased input power requirements, reducing the overall second-law efficiency (Fig. 13). Compared to layered LaFeSi-based AMRs with the same bed porosity [37], recently tested at DTU, the present system produced larger temperature spans. It is also obvious that the LaFeSi-

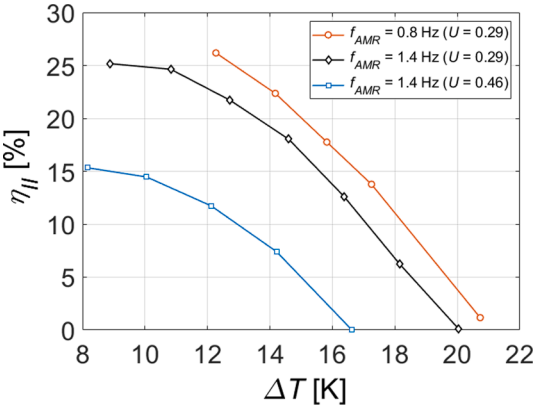

Fig. 13. Second-law efficiency as a function of the reservoir temperature span for different AMR frequencies.

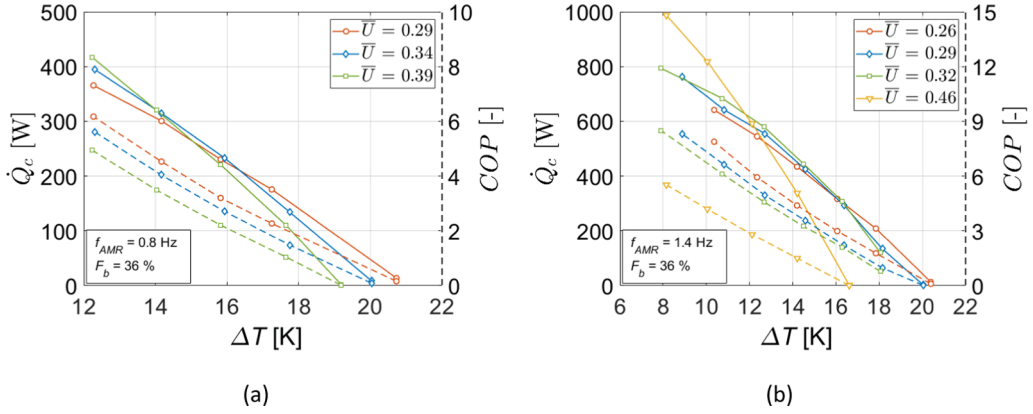

Fig. 12. (a) Cooling power (solid lines) and cooling COP (dashed lines) vs. the temperature span for a range of utilization factors. (b) Cooling power (solid lines) and cooling COP (dashed lines) vs. the temperature span for a range of utilization factors.

based AMRs (already at 0.5 Hz) showed a steeper slope in the cooling curve than the Gd-based AMRs, i.e., the LaFeSi-based AMRs can produce more cooling power at smaller spans. Hence, at higher spans, the performance is limited by their small adiabatic temperature change. The second-law efficiencies obtained in this study are less than those of conventional vapor compression cooling equipment. When comparing magnetocaloric cooling with vapor compression systems, however, one has to consider the continuous advancements made in these mature systems over time, with efficiencies improving from around 32% in 2007 to over 50% today [63].

4.7. Further optimization of the AMR cooling efficiency

An important strategy for building more efficient AMR designs is to identify and determine the causes and magnitude of inefficiencies in the cooling system. Most cooling devices often operate outside of their optimum operating envelope, resulting in reduced efficiency and negative environmental effects. The thermodynamic efficiency of the AMR cooling device may be improved by minimizing different sources of losses, such as magnetic, thermal, hydrodynamic, and mechanical losses. Inefficiencies in the motor, gearbox, and drive train, as well as frictional drag on the bearings, all contribute to the magnitude of the magnetic power. By selecting a more efficient motor and transmission system, the magnetic work may be lower and thereby increase the *COP*.

Viscous dissipation as a result of an increased pressure drop along the AMR bed represents another loss mechanism that can reduce the AMR performance. When compared to a rectangular geometry, the trapezoid-shaped regenerator geometry with a tapering angle of -10° already lowers the viscous losses [64]. In addition, it has been shown that advanced regenerator geometry designs, such as triangular microchannels [65] and parallel plates [66], can work more efficiently than packed-bed AMRs filled with spheres owing to the reduced pressure drop.

Packed beds with spherical particles also suffer from demagnetization losses, which can further impair the AMR performance. Because the demagnetization factor of a single sphere is 1/3, the demagnetization factor of a packed bed AMR can be significantly higher than if it had been solid [67]. If the refrigerant mass is fixed, employing multiple but narrower AMR beds increases the cooling capacity and decreases demagnetization losses, but increases the *COP* owing to the increased valve power consumption compared to fewer (but wider) regenerator beds [68].

The heat generated in the MCM due to magnetic and thermal hysteresis is another source of irreversible entropy production that reduces the efficiency of the AMR cooling cycle. The magnitude of the magnetic hysteresis loss can be estimated by measuring isothermal magnetization curves, where the heat produced in an AMR cycle corresponds to the hysteresis loop area [69]. However, Gd with a second-order phase transition (SOPT) exhibits no magnetic hysteresis loss [70]. The width of the thermal hysteresis has a considerable effect on the reversibility of the MCE, which is crucial for magnetic refrigeration. As a result, minimizing thermal hysteresis losses is critical for improving the efficiency of AMR cooling systems [70]. Gd also has no thermal hysteresis [71], while materials with a first-order phase transition have intrinsic thermal hysteresis [72], which may be tunable by modifying their composition or the annealing conditions [73].

Another loss mechanism that can prevent an efficient heat transfer between the AMR and the thermal reservoirs, resulting in a penalty on the AMR's thermal performance, is the empty (void) volume on either side of the AMR, i.e., the AMR dead volume [25,74–76]. To increase the cooling capacity and hence maximize the AMR performance, the dead volume should be minimized [76]. The total estimated dead volume on either side of the AMR is given in Ref. [36], and additional void volume formation in the AMR was minimized by compressing the particle bed. Furthermore, the fluid entering and exiting the AMR was divided into two separate channels with equal sizes to avoid variations in the fluid flow velocity [77], causing flow maldistributions that were shown to significantly impact the AMR effectiveness [75,78,79].

The heat transfer (or heat leakage) from the AMR to the surrounding due to forced and natural convection results in irreversible thermal parasitic losses, which are detrimental to the AMR effectiveness [12,25,80]. These losses are significant at larger temperature spans when the regenerator cold end operates at temperatures below room temperature [12]. As heat must be transferred to and from the wall from the refrigerant and the working fluid, the regenerator housing wall acts as a passive regenerator, which surrounds the actual solid regenerator matrix. For wall materials with sufficient thermal diffusivity, axial conduction in the wall can affect the regenerator performance. In addition, if the thermal mass of the wall is greater than that of the solid, thermal energy will tend to transfer to the wall rather than the solid, causing a greater impact on the AMR performance [81]. In the present study, the thermal mass of the nylon housing wall was reduced by incorporating cavities in the wall while still assuring both good thermal insulation of the housing and sufficient deformation of the housing under operating pressure. The heat loss from the AMR to the iron ring was reduced by embossing the housing bottom surface. The heat loss through the metal lid on top of the regenerator to the environment was reduced by placing a silicon foam sheet between the sphere-packed bed and the lid [77]. Because of point contacts, sphere-packed beds have lower axial heat conduction losses than beds with parallel plates [67].

5. Conclusion

An experimental analysis of the performance of a rotary magnetocaloric device with single-layered gadolinium-based regenerators was performed. Different sets of operating conditions were tested and their influence on the thermodynamic efficiency was evaluated. The device is able to quickly establish a temperature span of 16.6 K starting from room temperature within 25 min. It was shown that the performance of the multi-bed device is greatly reduced when large variations in the bed flow resistance occur, and blow fraction adjustments of individual beds can correct those and improve the performance by more than 70%. The efficiency of the active magnetic regenerator system is not largely impacted by the working temperature. At a cycle frequency of 1.4 Hz, a utilization of 0.33, and a working temperature of 301 K, the device produced a cooling capacity of 344 W over a 16 K span at a coefficient of performance of 2.3. The highest second-law efficiency of 39.2% was obtained for a utilization of 0.39, a frequency of 0.5 Hz, and a hot reservoir temperature of 301 K. At this condition, the device produced a cooling power of 444 W over a span of 7.3 K and a coefficient of performance of 15.9. The most limiting factors for achieving higher cooling performance were the flow rate limit and the solenoid valve operation at higher frequencies. Future studies will focus on validating the experimental results of the magnetocaloric device with a numerical model.

Declaration of Competing Interest

The authors declare that they have no known competing financial interests or personal relationships that could have appeared to influence the work reported in this paper.

Acknowledgements

This work was in part financed by the RES4Build project, which received funding from the European Union's Horizon 2020 research and innovation program under grant agreement No.814865.

Appendix A. Supplementary material

The supplementary material for this article can be found online at doi:10.11583/DTU.17025893.

References

[1] P. Weiss, A. Piccard, Le phénomène magnétocalorique, J. Phys. Theor. Appl. 7 (1917) 103–109.
[2] G.V. Brown, Magnetic heat pumping near room temperature, J. Appl. Phys. 47 (1976) 3673–3680, https://doi.org/10.1063/1.323176.
[3] S.Y. Dan'Kov, A.M. Tishin, V.K. Pecharsky, K.A. Gschneidner Jr., Magnetic phase transitions and the magnetothermal properties of gadolinium, Phys. Rev. B. 57 (1998) 3478–3490, https://doi.org/10.1103/PhysRevB.57.3478.
[4] A. Smith, C.R.H. Bahl, R. Bjørk, K. Engelbrecht, K.K. Nielsen, N. Pryds, Materials challenges for high performance magnetocaloric refrigeration devices, Adv. Energy Mater. 2 (2012) 1288–1318, https://doi.org/10.1002/aenm.201200167.
[5] A. Tura, A. Rowe, Permanent magnet magnetic refrigerator design and experimental characterization, Int. J. Refrig. 34 (2010) 628–639, https://doi.org/10.1016/j.ijrefrig.2010.12.009.
[6] K. Engelbrecht, D. Eriksen, C.R.H. Bahl, R. Bjørk, J. Geyti, J.A. Lozano, K. K. Nielsen, F. Saxild, A. Smith, N. Pryds, Experimental results for a novel rotary active magnetic regenerator, Int. J. Refrig. 5 (2012) 3–10, https://doi.org/10.1016/j.ijrefrig.2012.05.003.
[7] Z. Li, J. Shen, K. Li, X. Gao, X. Guo, W. Dai, Assessment of three different gadolinium-based regenerators in a rotary-type magnetic refrigerator, Appl. Therm. Eng. 153 (2019) 159–167, https://doi.org/10.1016/j.applthermaleng.2019.02.100.
[8] T. Kawanami, S. Hirano, K. Fumoto, S. Hirasawa, Evaluation of fundamental performance on magnetocaloric cooling with active magnetic regenerator, Appl. Therm. Eng. 31 (2011) 1176–1183, https://doi.org/10.1016/j.applthermaleng.2010.12.017.
[9] J. Tušek, S. Zupan, A. Šarlah, I. Prebil, A. Poredoš, Development of a rotary magnetic refrigerator, Int. J. Refrig. 33 (2010) 294–300, https://doi.org/10.1016/j.ijrefrig.2009.11.003.
[10] D. Eriksen, K. Engelbrecht, C.R.H. Bahl, R. Bjørk, K.K. Nielsen, A.R. Insinga, N. Pryds, Design and experimental tests of a rotary active magnetic regenerator prototype, Int. J. Refrig. 58 (2015) 14–21, https://doi.org/10.1016/j.ijrefrig.2015.05.004.
[11] C. Aprea, A. Greco, A. Maiorino, C. Masselli, The energy performances of a rotary permanent magnet magnetic refrigerator, Int. J. Refrig. 61 (2016) 1–11, https://doi.org/10.1016/j.ijrefrig.2015.09.005.
[12] J.A. Lozano, K. Engelbrecht, C.R.H. Bahl, K.K. Nielsen, D. Eriksen, U.L. Olsen, J. R. Barbosa Jr., A. Smith, A.T. Prata, N. Pryds, Performance analysis of a rotary active magnetic refrigerator, Appl. Energy. 111 (2013) 669–680, https://doi.org/10.1016/j.apenergy.2013.05.039.
[13] J. Tušek, A. Kitanovski, S. Zupan, I. Prebil, A. Poredoš, A comprehensive experimental analysis of gadolinium active magnetic regenerators, Appl. Therm. Eng. 53 (2013) 57–66, https://doi.org/10.1016/j.applthermaleng.2013.01.015.
[14] D. Eriksen, K. Engelbrecht, C.R.H. Bahl, R. Bjørk, Exploring the efficiency potential for an active magnetic regenerator, Sci. Technol. Built Environ. 22 (2016) 527–533, https://doi.org/10.1080/23744731.2016.1173495.
[15] C.R.H. Bahl, K. Engelbrecht, D. Eriksen, J.A. Lozano, R. Bjørk, J. Geyti, K. K. Nielsen, A. Smith, N. Pryds, Development and experimental results from a 1 kW prototype AMR, Int. J. Refrig. 37 (2013) 78–83, https://doi.org/10.1016/j.ijrefrig.2013.09.001.
[16] S. Lionte, M. Risser, C. Muller, A 15 kW magnetocaloric proof-of-concept unit: initial development and first experimental results, Int. J. Refrig. 122 (2020) 256–265, https://doi.org/10.1016/j.ijrefrig.2020.09.019.
[17] D.S. Arnold, A. Tura, A. Ruebsaat-Trott, A. Rowe, Design improvements of a permanent magnet active magnetic refrigerator, Int. J. Refrig. 37 (2014) 99–105, https://doi.org/10.1016/j.ijrefrig.2013.09.024.
[18] T. Okamura, N. Hirano, Improvement of the Performance of Room Temperature Magnetic Refrigerator using Gd-alloy, J. Japan Soc. Appl. Electromagn. Mech. 21 (2013) 10–14, https://doi.org/10.14243/jsaem.21.10.
[19] A. Kitanovski, J. Tušek, U. Tomc, U. Plaznik, M. Ožbolt, A. Poredoš. Magnetocaloric Energy Conversion: From Theory to Applications, Springer, 2015, ISBN 978-3-319-08740-5.
[20] X.N. He, M.Q. Gong, H. Zhang, W. Dai, J. Shen, J.F. Wu, Design and performance of a room-temperature hybrid magnetic refrigerator combined with Stirling gas refrigeration effect, Int. J. Refrig. 6 (2013) 2–8, https://doi.org/10.1016/j.ijrefrig.2013.03.014.
[21] C. Aprea, A. Greco, A. Maiorino, R. Mastrullo, A. Tura, Initial experimental results from a rotary permanent magnet magnetic refrigerator, Int. J. Refrig. 43 (2014) 111–122, https://doi.org/10.1016/j.ijrefrig.2014.03.014.
[22] Z. Cheng, H. Jiaohong, Y. Hongwei, J. Peiyu, C. Juan, L. Cuilan, L. Zhaojie, Z. Yingde, Design and research of the room temperature magnetic wine cabinet, Refrig. Sci. Technol. (2016) 63–66, https://doi.org/10.18462/iir.thermag.2016.0090.
[23] P.V. Trevizoli, A.T. Nakashima, G.F. Peixer, J.R. Barbosa Jr., Performance evaluation of an active magnetic regenerator for cooling applications – part I : Experimental analysis and thermodynamic performance, Int. J. Refrig. 72 (2016) 192–205, https://doi.org/10.1016/j.ijrefrig.2016.07.009.
[24] P.V. Trevizoli, J.A. Lozano, G.F. Peixer, J.R. Barbosa Jr., Design of nested Halbach cylinder arrays for magnetic refrigeration applications, J. Magn. Magn. Mater. 395 (2015) 109–122, https://doi.org/10.1016/j.jmmm.2015.07.023.
[25] P.V. Trevizoli, A.T. Nakashima, J.R. Barbosa Jr., Performance evaluation of an active magnetic regenerator for cooling applications – part II: Mathematical modeling and thermal losses, Int. J. Refrig. 72 (2016) 206–217, https://doi.org/10.1016/j.ijrefrig.2016.07.010.
[26] M.A. Benedict, S.A. Sherif, D.G. Beers, M.G. Schroeder, Design and performance of a novel magnetocaloric heat pump, Sci. Technol. Built Environ. 22 (2016) 520–526, https://doi.org/10.1080/23744731.2016.1185889.
[27] J.A. Lozano, M.S. Capovilla, P.V. Trevizoli, K. Engelbrecht, C.R.H. Bahl, J. R. Barbosa Jr., Development of a novel rotary magnetic refrigerator, Int. J. Refrig. 68 (2016) 187–197, https://doi.org/10.1016/j.ijrefrig.2016.04.005.
[28] B. Huang, J.W. Lai, D.C. Zeng, Z.G. Zheng, B. Harrison, A. Oort, N.H. van Dijk, E. Brück, Development of an experimental rotary magnetic refrigerator prototype, Int. J. Refrig. 104 (2019) 42–50, https://doi.org/10.1016/j.ijrefrig.2019.04.029.
[29] RES4BUILD, (2021). https://res4build.eu/about/project-overview/ (accessed October 8, 2021).
[30] D. Eriksen, K. Engelbrecht, C.R.H. Bahl, R. Bjørk, K.K. Nielsen, Effects of flow balancing on active magnetic regenerator performance, Appl. Therm. Eng. 103 (2016) 1–8, https://doi.org/10.1016/j.applthermaleng.2016.03.001.
[31] D. Eriksen, K. Engelbrecht, C.R.H. Bahl, R. Bjørk, K.K. Nielsen, A.R. Insinga, S. Dall'Olio, N. Pryds, Experimental studies with an active magnetic regenerating refrigerator, Refrig. Sci. Technol. (2015) 926–933, https://doi.org/10.18462/iir.icr.2015.0812.
[32] R. Teyber, P.V. Trevizoli, I. Niknia, T.V. Christiaanse, P. Govindappa, A. Rowe, Experimental performance investigation of an active magnetic regenerator subject to different fluid flow waveforms, Int. J. Refrig. 74 (2017) 38–46, https://doi.org/10.1016/j.ijrefrig.2016.10.001.
[33] A.T.D. Nakashima, S.L. Dutra, P.V. Trevizoli, J.R. Barbosa Jr., Influence of the flow rate waveform and mass imbalance on the performance of active magnetic regenerators. Part II: Numerical simulation, Int. J. Refrig. 93 (2018) 159–168, https://doi.org/10.1016/j.ijrefrig.2018.07.005.
[34] A.T.D. Nakashima, S.L. Dutra, P.V. Trevizoli, J.R. Barbosa Jr., Influence of the flow rate waveform and mass imbalance on the performance of active magnetic regenerators. Part I: Experimental analysis, Int. J. Refrig. 93 (2018) 236–248, https://doi.org/10.1016/j.ijrefrig.2018.07.004.
[35] J. Holladay, R. Teyber, K. Meinhardt, E. Polikarpov, E. Thomsen, C. Archipley, J. Cui, J. Barclay, Investigation of bypass fluid flow in an active magnetic regenerative liquefier, Cryogenics (Guildf). 93 (2018) 34–40, https://doi.org/10.1016/j.cryogenics.2018.05.010.
[36] S. Dall'Olio, M. Masche, J. Liang, A.R. Insinga, D. Eriksen, R. Bjørk, K.K. Nielsen, A. Barcza, H.A. Vieyra, N. v. Beek, H.N. Bez, K. Engelbrecht, C.R.H. Bahl, Novel design of a high efficiency multi-bed active magnetic regenerator heat pump, Int. J. Refrig. 132 (2021) 243–254, https://doi.org/10.1016/j.ijrefrig.2021.09.007.
[37] M. Masche, J. Liang, S. Dall'Olio, K. Engelbrecht, C.R.H. Bahl, Performance analysis of a high-efficiency multi-bed active magnetic regenerator device, Appl. Therm. Eng. 183 (2021) 117569, https://doi.org/10.1016/j.applthermaleng.2021.117569.
[38] F.P. Fortkamp, D. Eriksen, K. Engelbrecht, C.R.H. Bahl, J.A. Lozano, J. R. Barbosa Jr., Experimental investigation of different fluid flow profiles in a rotary multi-bed active magnetic regenerator device, Int. J. Refrig. 91 (2018) 46–54, https://doi.org/10.1016/j.ijrefrig.2018.04.019.
[39] S. Ergun, Fluid Flow through Packed Column, Chem. Eng. Prog. 48 (1952) 89–94.
[40] I.F. Macdonald, M.S. El-Sayed, K. Mow, F.A.L. Dullien, Flow through Porous Media—the Ergun Equation Revisited, Ind. Eng. Chem. Fundam. 18 (1979) 199–208, https://doi.org/10.1021/i160071a001.
[41] H. Neves Bez, K. Navickaitė, T. Lei, K. Engelbrecht, A. Barcza, C.R.H. Bahl, Epoxy-bonded La(Fe,Mn,Si)13Hz as a multi layered active magnetic regenerator, in: 7th Int. Conf. Caloric Cool., Torino, Italy, 2016. doi:10.18462/iir.thermag.2016.0147.
[42] M.S. Kamran, H.O. Ahmad, M. Asim, N. Hayat, Performance Analysis of Amicrochannel Amr Magnetic Refrigerator Using Different Heat Transfer Fluids, World Appl. Sci. J. 35 (2017) 1658–1665, https://doi.org/10.5829/idosi.wasj.2017.1658.1665.
[43] Engineering equation solver, F-Chart Software, V10.889, 2020.
[44] J. Abrahamsson, J.G. de Oliveira, J. de Santiago, J. Lundin, H. Bernhoff, On the Efficiency of a Two-Power-Level Flywheel-Based All-Electric Driveline, Energies. 5 (2012) 2794–2817, https://doi.org/10.3390/en5082794.
[45] A. La Rocca, P.H. Connor, Z. Xu, C.N. Eastwick, S.J. Pickering, C. Gerada. Thermo-Mechanical Modelling of Bearing Chambers of a High-Speed Starter/Generator, IEEE, 2019, pp. 322–328, https://doi.org/10.1109/IEMDC.2019.8785357.
[46] A. Rowe, Configuration and performance analysis of magnetic refrigerators, Int. J. Refrig. 34 (2011) 168–177, https://doi.org/10.1016/j.ijrefrig.2010.08.014.
[47] H.W. Coleman, W.G. Steele. Experimentation, validation, and uncertainty analysis for engineers, John Wiley & Sons, 2018.
[48] Cadena, JA Lozano, Designing a rotary magnetic refrigerator. PhD thesis, Federal University of Santa Catarina, Bazil 2015.
[49] P.M. de Oliveira. On air-water two-phase flows in return bends. Master's thesis, Federal University of Santa Catarina, Brazil, 2013.
[50] B.P. Vieira, H.N. Bez, M. Kuepferling, M.A. Rosa, D. Schafer, C.C. Plá Cid, H. A. Vieyra, V. Basso, J.A. Lozano, J.R. Barbosa Jr., Magnetocaloric properties of spheroidal La(Fe, Mn, Si)13Hy granules and their performance in epoxy-bonded active magnetic regenerators, Appl. Therm. Eng. 183 (2021), 116185, https://doi.org/10.1016/j.applthermaleng.2020.116185.
[51] A.T.D. Nakashima, S.L. Dutra, J.R. Barbosa Jr., Experimental Evaluation of the Flow Imbalance in an Active Magnetic Experimental, 9th World Conf. Exp. Heat Transf. Fluid Mech. Thermodyn. (2017).
[52] A.T.D. Nakashima, F.P. Fortkamp, N.M. de Sá, V.M.A. dos Santos, G. Hoffmann, G. F. Peixer, S.L. Dutra, M.C. Ribeiro, J.A. Lozano, J.R.B. Jr, A Magnetic Wine Cooler Prototype, Int. J. Refrig. 122 (2020) 110–121, https://doi.org/10.1016/j.ijrefrig.2020.11.015.

[53] P. Li, M. Gong, G. Yao, J. Wu, A practical model for analysis of active magnetic regenerative refrigerators for room temperature applications, Int. J. Refrig. 29 (2006) 1259–1266, https://doi.org/10.1016/j.ijrefrig.2006.07.021.
[54] J. Tušek, A. Kitanovski, U. Tomc, C. Favero, A. Poredoš, Experimental comparison of multi-layered La-Fe-Co-Si and single-layered Gd active magnetic regenerators for use in a room-temperature magnetic refrigerator, Int. J. Refrig. 37 (2014) 117–126, https://doi.org/10.1016/j.ijrefrig.2013.09.003.
[55] J. He, J. Wu, B. Lu, C. Liu, Comparative study on the series, parallel and cascade cycles of a multi-mode room temperature magnetic refrigeration system, Int. J. Refrig. 117 (2020) 94–103, https://doi.org/10.1016/j.ijrefrig.2020.04.011.
[56] S. Qian, L. Yuan, J. Yu, G. Yan, Variable load control strategy for room-temperature magnetocaloric cooling applications, Energy. 153 (2018) 763–775, https://doi.org/10.1016/j.energy.2018.04.104.
[57] K.K. Nielsen, R. Bjørk, J.B. Jensen, C.R.H. Bahl, N. Pryds, A. Smith, A. Nordentoft, J. Hattel, Magnetic cooling at Risø DTU, arXiv preprint arXiv:0902.0812 (2009) 4–11.
[58] K.K. Nielsen, C.R.H. Bahl, A. Smith, N. Pryds, J. Hattel, A comprehensive parameter study of an active magnetic regenerator using a 2D numerical model, Int. J. Refrig. 33 (2010) 753–764, https://doi.org/10.1016/j.ijrefrig.2009.12.024.
[59] M. Balli, O. Sari, C. Mahmed, C. Besson, P. Bonhote, D. Duc, J. Forchelet, A pre-industrial magnetic cooling system for room temperature application, Appl. Energy. 98 (2012) 556–561, https://doi.org/10.1016/j.apenergy.2012.04.034.
[60] Y. Chiba, Y. Marif, N. Henini, A. Tlemcani, Modeling of Magnetic Refrigeration Device by Using Artificial Neural Networks Approach, Int. J. Energy Optim. Eng. 10 (2021) 68–76, https://doi.org/10.4018/IJEOE.2021100105.
[61] Y. Chiba, A. Smaili, O. Sari, Enhancements of thermal performances of an active magnetic refrigeration device based on nanofluids, Mechanics 23 (2017) 31–38, https://doi.org/10.5755/j01.mech.23.1.13452.
[62] Y. Chiba, Y. Marif, A. Boukaoud, D. Sebbar. Performance Enhancement of a Magnetic Refrigeration Device based on TiO_2 used as Secondary Fluid, IEEE, 2019, pp. 1–4, https://doi.org/10.1109/IRSEC48032.2019.9078233.
[63] J. Steven Brown, P.A. Domanski, Review of alternative cooling technologies, Appl. Therm. Eng. 64 (2014) 252–262, https://doi.org/10.1016/j.applthermaleng.2013.12.014.
[64] S. Dall'Olio, T. Lei, K. Engelbrecht, C.R.H. Bahl, The effect of tapering on a magnetocaloric regenerator bed, Int. J. Refrig. 84 (2017) 300–308, https://doi.org/10.1016/j.ijrefrig.2017.08.012.
[65] J. Liang, K. Engelbrecht, K.K. Nielsen, K. Loewe, H. Vieyra, A. Barcza, C.R.H. Bahl, Performance assessment of a triangular microchannel active magnetic regenerator, Appl. Therm. Eng. 186 (2021) 116519, https://doi.org/10.1016/j.applthermaleng.2020.116519.
[66] A. Šarlah, J. Tušek, A. Poredoš, Comparison of thermo-hydraulic properties of heat regenerators applicable to active magnetic refrigerators, Stroj. Vestnik/Journal, Mech. Eng. 58 (2012) 16–22, https://doi.org/10.5545/sv-jme.2010.250.
[67] P.V. Trevizoli, T.V. Christiaanse, P. Govindappa, I. Niknia, R. Teyber, J. R. Barbosa Jr., A. Rowe, Magnetic heat pumps: An overview of design principles and challenges, Sci. Technol. Built Environ. 22 (2016) 507–519, https://doi.org/10.1080/23744731.2016.1171632.
[68] F.P. Fortkamp, G.B. Lang, J.A. Lozano, J.R. Barbosa Jr., Design trade-offs for an active magnetic regenerator device, Appl. Therm. Eng. 165 (2020), 114467, https://doi.org/10.1016/j.applthermaleng.2019.114467.
[69] L. von Moos, Hysteresis in magnetocaloric materials : an experimental and modelling approach, PhD Thesis. Department of Energy Conversion and Storage, Technical University of Denmark (2014).
[70] O. Gutfleisch, T. Gottschall, M. Fries, D. Benke, I. Radulov, K.P. Skokov, H. Wende, M. Gruner, M. Acet, P. Entel, M. Farle, Mastering hysteresis in magnetocaloric materials, Philos. Trans. R. Soc. A Math. Phys. Eng. Sci. 374 (2016), https://doi.org/10.1098/rsta.2015.0308, 20150308.
[71] F.J. Jelinek, E.D. Hill, B.C. Gerstein, Initial susceptibility investigation of magnetic transitions in several rare earth metals: Thermal hysteresis in ferromagnetic transitions, J. Phys. Chem. Solids. 26 (1965) 1475–1488, https://doi.org/10.1016/0022-3697(65)90046-6.
[72] V. Franco, J.S. Blázquez, B. Ingale, A. Conde, The Magnetocaloric Effect and Magnetic Refrigeration Near Room Temperature: Materials and Models, Annu. Rev. Mater. Res. 42 (2012) 305–342, https://doi.org/10.1146/annurev-matsci-062910-100356.
[73] N.T. Trung, Z.Q. Ou, T.J. Gortenmulder, O. Tegus, K.H.J. Buschow, E. Brück, Tunable thermal hysteresis in MnFe(P, Ge) compounds, Appl. Phys. Lett. 94 (2009) 102513, https://doi.org/10.1063/1.3095597.
[74] P.V. Trevizoli, J.R. Barbosa Jr., Thermal-hydraulic behavior and influence of carryover losses in oscillating-flow regenerators, Int. J. Therm. Sci. 113 (2017) 89–99, https://doi.org/10.1016/j.ijthermalsci.2016.11.002.
[75] P.V. Trevizoli, M.S. Capovilla, G.F. Peixer, A.T. Nakashima, J.A. Lozano, J. R. Barbosa Jr., Influence of void volume and inlet flow maldistribution on the performance of thermal regenerators, Refrig. Sci. Technol. (2016) 83–86, https://doi.org/10.18462/iir.thermag.2016.0102.
[76] I. Park, Y. Kim, S. Jeong, Development of the tandem reciprocating magnetic regenerative refrigerator and numerical simulation for the dead volume effect, Int. J. Refrig. 36 (2013) 1741–1749, https://doi.org/10.1016/j.ijrefrig.2013.03.012.
[77] S. Dall'Olio, D. Eriksen, K. Engelbrecht, A.R. Insinga, C.R.H. Bahl, Design, enhanced thermal and flow efficiency of a 2 kW active magnetic regenerator, in: 9th World Conf. Exp. Heat Transf. Fluid Mech. Thermodyn., 2017: pp. 1–10.
[78] K. Engelbrecht, J. Tušek, K.K. Nielsen, A. Kitanovski, C.R.H. Bahl, A. Poredoš, Improved modelling of a parallel plate active magnetic regenerator, J. Phys. D. Appl. Phys. 46 (2013), https://doi.org/10.1088/0022-3727/46/25/255002.
[79] K.K. Nielsen, K. Engelbrecht, C.R.H. Bahl, The influence of flow maldistribution on the performance of inhomogeneous parallel plate heat exchangers, Int. J. Heat Mass Transf. 60 (2013) 432–439, https://doi.org/10.1016/j.ijheatmasstransfer.2013.01.018.
[80] T. Lei, Modeling of active magnetic regenerators and experimental investigation of passive regenerators with oscillating flow, PhD Thesis, Department of Energy Conversion and Storage, Technical University of Denmark (2016).
[81] K.K. Nielsen, G.F. Nellis, S.A. Klein, Numerical modeling of the impact of regenerator housing on the determination of Nusselt numbers, Int. J. Heat Mass Transf. 65 (2013) 552–560, https://doi.org/10.1016/j.ijheatmasstransfer.2013.06.032.